Parameter estimation for inspiraling eccentric compact binaries including pericenter precession

Balázs Mikóczi, Bence Kocsis, Péter Forgács, and Mátyás Vasúth

Phys. Rev. D **86**, 104027 — Published 9 November 2012

DOI: 10.1103/PhysRevD.86.104027

Parameter estimation for inspiraling eccentric compact binaries including pericenter precession

Balázs Mikóczi[1], Bence Kocsis[2], Péter Forgács[1,3], and Mátyás Vasúth[1]
[1]Research Institute for Particle and Nuclear Physics,
Wigner RCP H-1525 Budapest 114, P.O. Box 49, Hungary
[2] Harvard-Smithsonian Center for Astrophysics,60 Garden St., Cambridge, MA 02138, USA and
[3]LMPT, CNRS-UMR 6083, Université de Tours, Parc de Grandmont, 37200 Tours, France

Inspiraling supermassive black hole binary systems with high orbital eccentricity are important sources for space-based gravitational wave (GW) observatories like the Laser Interferometer Space Antenna (LISA). Eccentricity adds orbital harmonics to the Fourier-transform of the GW signal and relativistic pericenter precession leads to a three-way splitting of each harmonic peak. We study the parameter estimation accuracy for such waveforms with different initial eccentricity using the Fisher matrix method and a Monte Carlo sampling of the initial binary orientation. The eccentricity improves the parameter estimation by breaking degeneracies between different parameters. In particular, we find that the source localization precision improves significantly for higher mass binaries due to eccentricity. The typical sky position errors are $\sim 1\,$deg for a nonspinning, $10^7\,M_\odot$ equal mass binary at redshift $z = 1$, if the initial eccentricity one year before merger is $e_0 \sim 0.6$. Pericenter precession does not affect the source localization accuracy significantly, but it does further improve the mass and eccentricity estimation accuracy systematically by a factor of 3–10 for masses between 10^6 and $10^7\,M_\odot$ for $e_0 \sim 0.3$.

PACS numbers: 04.30.Db, 04.80.Nn, 97.60.Lf

I. INTRODUCTION

The inspiral and merger of compact binary systems of black holes are important sources of gravitational waves (GWs) for the proposed space-based GW missions such as the Laser Interferometer Space Antenna (LISA) [1] or the European New Gravitational Wave Observatory (NGO/eLISA) [2]. The detectable frequency band for these instruments will be around 10^{-4}–10^{-1} Hz [3] which corresponds to the inspiral of two $(10^4 - 10^7)M_\odot$ black holes. As the sources detected by LISA/NGO will be loud with a large signal-to-noise ratio in general, an ideal method for parameter extraction is matched filtering [4].

An effective matched filtering requires an accurate model of the emitted GWs. In this technique the detected signal output is cross correlated with theoretical waveform templates. In particular, matched filtering is sensitive to the phase information of the waveform, and a high correlation between the signal and template allows one to make predictions on the source parameters [5, 6].

Many previous studies in the literature adopted waveforms generated by binaries on circular orbits (see [7–19] for LISA parameter estimation). This is due to the expectation that the orbit of the binary circularizes due to the emission of GWs [20, 21].

Nevertheless, there are a number of reasons to expect that at least some LISA sources may be eccentric. If the binary is embedded in a gaseous disk, it can remain eccentric until the final year of the inspiral [22–25]. The interaction of the supermassive black hole (SMBH) binary with a population of stars also increases the eccentricity [26–28]. The eccentricity can also be excited by the Kozai mechanism and relativistic orbital resonances in hierarchial triples [29–33] or by a triaxial potential [34, 35], and may be typical for extreme mass ratio inspirals [36, 37]. Further, black hole binaries in dense galactic nuclei formed by GW emission during close encounters remain very eccentric until merger [38, 39]. Population synthesis and binary evolutionary models show that a fraction of stellar compact object binaries may also be eccentric for ground based (Advanced LIGO/VIRGO and Einstein Telescope) and space-based detectors such as DECIGO [40].

Including eccentricity in the waveform may be essential for the detection of inspiraling eccentric binaries with matched filtering and to avoid a systematic bias in the parameter estimation [41]. Using circular templates to detect waveforms with eccentricities $e_0 \gtrsim 0.1$, leads to a significant loss of signal-to-noise ratio for ground-based detectors such as LIGO and VIRGO [42, 43]. A similar conclusion was reached for eccentric massive black hole binaries detected with LISA [44]. The orbital evolution and waveforms have been developed to first and second post-Newtonian (PN) order, including spin-orbit, spin-spin contributions for eccentric orbits [45–50].

To assess the astrophysical impact of planned GW instruments, it is essential to estimate the expected parameter measurement precision of typical GW sources. This may be done by injecting a simulated GW signal into synthetic detector noise and carrying out a Monte Carlo Markov Chain (MCMC) based matched filtering search for a parametrized template model to recover the posterior distribution function (PDF) of the estimated source parameters [51]. Porter and Sesana [44] investigated the case of low $(100M_\odot)$ and high $(10^4M_\odot)$ mass black hole binaries on eccentric orbits using non-spinning, restricted 2PN waveforms. They concluded that eccentricity can significantly bias the recovered parameters of the source for LISA if circular templates are used even if the eccentricity is as small as $e \sim 10^{-4}$. More recently, Key and Cornish [52] extended that study by using an effective 1.5PN waveform for inspiraling eccentric SMBHs (with $m \sim (10^5 - 10^7)M_\odot$) taking into account eccentricity and spin effects in the template model. They found that the eccentricity measurement errors are of order $\Delta e \sim 10^{-3}$ for a range of mass ratios and a particular choice of angular parameters.

Since the parameter space is large, 17 dimensional for an eccentric spinning binary, state of the art MCMC calculations are numerically too expensive to explore the full range of source parameters. However, for large signal to noise ratio (SNR), the PDF may be well approximated by an ellipsoid, and the parameter measurement errors can be estimated very efficiently using the Fisher matrix method [5, 41]. Using this method, it has been shown that different source inclinations and sky locations lead to a wide range of parameter measurement errors subtending many orders of magnitude [9–11, 14, 53]. In this study, we carry out a Fisher matrix analysis to investigate the possible range of parameter estimation errors for eccentric binaries.

Only a few of studies have investigated the LISA parameter estimation accuracy for eccentric inspiraling sources using the Fisher matrix method (c.f. [8–14, 53] for circular inspirals). Barack and Cutler [54] investigated the LISA errors for highly eccentric stellar mass compact objects inspiraling into a SMBH. They found that the influence of eccentricities on $\Delta\mathcal{M}/\mathcal{M} \sim 10^{-4}$ (error of the chirp mass), $\Delta e_0 \sim 10^{-4}$ (error of initial eccentricity) and $\Delta\Omega_S \sim 10^{-4}$ (angular resolution error) is not substantial, the error estimates do not differ much from those obtained for circular orbits [8]. However, they assumed only an arbitrarily chosen, single set of orientations, which may not be representative of the typical errors. Yunes et al. [55] provided ready-to-use analytic expressions for the Fourier waveform of moderately eccentric sources. They have shown that eccentricity increases the detectable mass range of GW detectors toward higher masses by enhancing the orbital harmonics [12, 13]. Yagi and Tanaka [56] investigated the LISA errors for various alternative theories of gravity for spinning, small-eccentricity inspiraling SMBH binaries ($e_0 \sim 0.01$ at 1 yr before merger), using restricted 2PN waveforms, neglecting higher orbital harmonics and apsidal precession in the waveform. They have found that the eccentricity and the spin-orbit interaction reduces the parameter errors by an order of magnitude for spinning SMBHs in massive graviton theories, but not in Brans-Dicke-type theories.

Neither of the previous systematic Fisher matrix studies of parameter errors included the effects of relativistic pericenter precession for eccentric sources. However, precession effects introduce an additional feature in the waveform, and have the potential to break the degeneracy between parameter errors [18]. In particular, spin-orbit precession has been shown to improve the source localization precision substantially during the last day of the inspiral [9, 11, 14]. Similarly, GR pericenter precession may also be expected to improve the LISA parameter measurement accuracy. In fact, since pericenter precession enters at a lower PN order, this improvement could take place well before the binary reaches merger. Localizing the source before merger could be used to provide triggers for electromagnetic (EM) facilities to search for the EM counterpart [19]. A coincident GW and EM observation of the same source could have far reaching astrophysical implications [16, 17, 19, 57]

In the present paper, we carry out a systematic parameter estimation study for inspiraling SMBH binaries, taking into account both orbital eccentricity and the relativistic pericenter precession effect. We account for the evolution of the semimajor axis and eccentricity in our waveforms to leading order due to GW emission [42, 54, 58, 59], but neglect higher order PN contributions and spin effects. We compute the waveform in the frequency-domain using the stationary phase approximation (SPA, see [55, 60–63]), and derive the signal-to-noise-ratio (SNR) and the Fisher information matrix using a Fourier-Bessel analysis for the parameter estimation of eccentric sources. To explore the possible range of parameter errors, we generate a Monte Carlo sample of binaries with random orientations and vary the masses and initial eccentricities systematically over a wide range relevant for LISA. We calculate the parameter errors for the standard three-arm LISA/NGO configuration as well as for a descoped detector configuration, where one of the two independent interferometers is removed.

In Sec. II we summarize the basic formulae describing eccentric waveforms in the leading, quadrupole approximation using a Fourier-Bessel decomposition. In Sec. III, we derive the frequency-domain waveforms and the LISA detector response. After a brief introduction of parameter estimation using the Fisher matrix method in Sec. IV, we present results for specific systems in Sec. V. We summarize our conclusions in Sec VI. Some details of the calculations are described in Appendix A and B.

We use geometrical units $G = c = 1$.

II. TIME DEPENDENT ECCENTRIC WAVEFORMS

To leading order, the waveform emitted by a binary moving on a Keplerian orbit can be computed by the quadrupole approximation. In this approach the observer (i.e. the interferometric detector) is assumed to be far from the source and higher order contributions, e.g. the effects of the spins and higher multipole moments, are neglected, but the orbit is corrected for the effect of *pericenter precession*. For such precessing Keplerian orbits, the eccentric waveforms are given in Ref. [58]. We have rewritten the leading order quadrupole tensor and transformed to the *transverse-traceless gauge*, which gives

$$h_\times(\phi) = -\frac{\mu m \cos\Theta}{a(1-e^2)D_L}\Big[(5e\sin\phi + 4\sin 2\phi + e\sin 3\phi)\cos 2\gamma - \left(5e\cos\phi + 4\cos 2\phi + e\cos 3\phi + 2e^2\right)\sin 2\gamma\Big] , \tag{1}$$

$$h_+(\phi) = -\frac{\mu m\left(1+\cos^2\Theta\right)}{a(1-e^2)D_L}\left[\left(\frac{5e}{2}\cos\phi + 2\cos 2\phi + \frac{e}{2}\cos 3\phi + e^2\right)\cos 2\gamma + \left(\frac{5e}{2}\sin\phi + 2\sin 2\phi + \frac{e}{2}\sin 3\phi\right)\sin 2\gamma + \left(e\cos\phi + e^2\right)\frac{\sin^2\Theta}{1+\cos^2\Theta}\right] . \tag{2}$$

Here ϕ is the true anomaly, which describes the azimuthal angle from pericenter along the orbit as shown in Fig. 1, γ is the azimuthal angle of pericenter relative to the coordinate system x-axis in the orbital plane, e is the orbital eccentricity, a is the semimajor axis, D_L is the luminosity distance, Θ is the inclination (the angle between the orbital plane and the line of sight to the observer), and $m = m_1 + m_2$, $\mu = m_1 m_2/m$ are the total and reduced masses (Fig.1). Using the well-known Fourier-Bessel decomposition, the polarization states can be expressed as a sum of harmonics of the orbital frequency [61]

$$\widetilde{h}_\times(t) = -h\cos\Theta\sum_n \left[B_n^- \sin\Phi_{n+}^t + B_n^+ \sin\Phi_{n-}^t\right] , \tag{3}$$

$$\widetilde{h}_+(t) = -\tfrac{h}{2}\sum_n \Big[\sin^2\Theta A_n \cos\Phi_n^t + \left(1+\cos^2\Theta\right)\left(B_n^+\cos\Phi_{n-}^t - B_n^-\cos\Phi_{n+}^t\right)\Big] \tag{4}$$

Here $h = 4\mu m (aD_L)^{-1}$ is the amplitude, $B_n^\pm = \left(S_n \pm C_n\right)/2$ and A_n are linear combinations of the Bessel-functions of the first-kind ($J_n(ne)$) and their derivatives,

$$\begin{aligned} S_n &= -\frac{2\left(1-e^2\right)^{1/2}}{e} n^{-1} J_n'(ne) + \frac{2\left(1-e^2\right)^{3/2}}{e^2} n J_n(ne) , \\ C_n &= -\frac{2-e^2}{e^2} J_n(ne) + \frac{2\left(1-e^2\right)}{e} J_n'(ne) , \\ A_n &= J_n(ne) , \end{aligned} \tag{5}$$

where a prime denotes the derivative, i.e. $J_n'(ne) \equiv n\left[J_{n-1}(ne) + J_{n+1}(ne)\right]/2$. The phase functions in Eqs. (3–4) are

$$\Phi_n^t = nl , \tag{6}$$

$$\Phi_{n\pm}^t = nl \pm 2\gamma , \tag{7}$$

where l is the mean anomaly which is defined by the Kepler equation

$$l = \xi - e\sin\xi = 2\pi\nu(t - t_0) . \tag{8}$$

In the Kepler equation ξ is the eccentric anomaly and $\nu = T^{-1}$ is the Keplerian orbital frequency (here $T = 2\pi m^{-1/2} a^{3/2}$ is the Newtonian radial orbital period) and t_0 is the time of pericenter passage (thereafter we set $t_0 = 0$). Equations (6–7) show that the phase splits into a triplet due to the pericenter position γ. If the pericenter precesses, a triplet of frequencies appear in Fourier space for each harmonic [61, 62]. Note that Eq. (8) is approximately valid during an orbit as long as $v/c \ll 1$ and $\nu =$ constant, but this equation requires modifications on large timescales where the binary inspirals (see Eqs. 12–13 below) or at small separations where the 1PN treatment breaks down.

Pericenter precession leads to a time-dependent angle of pericenter, which may be written as $\gamma(t) = \gamma_0 + \gamma(t)$ where γ_0 is the initial angle of pericenter (Fig. 1). Henceforth we adopt pericenter precession from the classical relativistic motion and assume the adiabatic evolution of the orbital parameters. These effects are averaged over one radial oscillation period, i.e. $\langle\dot\gamma\rangle = \Delta\gamma/T$, where $\Delta\gamma = 6\pi m[a(1-e^2)]^{-1}$ is the angle of precession for an eccentric orbit governed by the geodesic equation of the Schwarzschild geometry (see e.g. [64]). In the following we shall drop $\langle\rangle$ for the average quantities, so we write

$$\dot\gamma = \frac{3m^{3/2}}{a^{5/2}(1-e^2)} = \frac{3m^{2/3}\left(2\pi\nu\right)^{5/3}}{(1-e^2)} . \tag{9}$$

The 2.5PN leading order adiabatic evolution of the orbital parameters due to gravitational radiation averaged over one radial period are [21]

$$\dot\nu = \frac{48\mathcal{M}^{5/3}(2\pi\nu)^{11/3}}{5\pi(1-e^2)^{7/2}}\left(1 + \frac{73}{24}e^2 + \frac{37}{96}e^4\right) , \tag{10}$$

$$\dot e = -\frac{304\mathcal{M}^{5/3}(2\pi\nu)^{8/3}}{15(1-e^2)^{5/2}} e\left(1 + \frac{121}{304}e^2\right) , \tag{11}$$

where $\mathcal{M} = \mu^{3/5}m^{2/5}$ is the chirp mass (we used Kepler's third law, i.e. $\nu = \left(2\pi\right)^{-1} m^{1/2} a^{-3/2}$).

For an inspiraling system, the phase functions are $\Phi_n^t = 2\pi n\int_{-\infty}^t \nu(t')dt'$ and $\Phi_{n\pm}^t = \Phi_n \pm 2\gamma_0 \pm 2\int_{-\infty}^t \dot\gamma(t')dt'$, Eqs. (6), (7), are generalized as (here the "t" index is suppressed in $\Phi_n^t, \Phi_{n\pm}^t$)

$$\Phi_n = 2\pi n\int_{-\infty}^{\nu(t)} \frac{\nu}{\dot\nu} d\nu , \tag{12}$$

$$\Phi_{n\pm} = \Phi_n \pm 2\gamma_0 \pm 2\int_{-\infty}^{\nu(t)} \frac{\dot\gamma}{\dot\nu} d\nu , \tag{13}$$

FIG. 1. The geometry of an eccentric orbit. The coordinate system (x, y, z) is defined by the initial orbit, where the x-axis points in the direction of the pericenter and the z-axis is parallel to the orbital angular momentum vector. In the reduced Kepler problem the body with mass $\mu = m_1 m_2/m$ is orbiting the central mass $m = m_1 + m_2$, the separation vector is $r = a_0(1-e_0^2)/(1+e_0\cos\phi)$ where e_0 is the orbital eccentricity, $a_0 = m^{1/3}(2\pi\nu_0)^{2/3}$ (here ν_0 is the orbital frequency) is the semimajor axis, ϕ is the true anomaly is the angle between pericenter and the separation vector) and γ_0 is the pericenter position. The Kepler equation determines the evolution of the time parameter: $\xi - e_0\sin\xi = 2\pi\nu_0(t-t_0)$ where ξ is the eccentric anomaly ($\tan\xi/2 = \sqrt{(1-e_0)/(1+e_0)}\tan\phi/2$). The adiabatic evolution of the eccentric orbit is driven by the pericenter precession (1PN effect) and the inspiral (2.5PN effect) of the compact binary due to gravitational radiation.

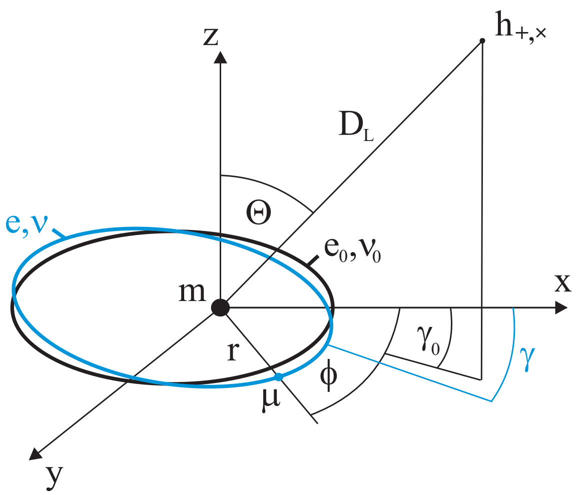

$\Phi_{n\pm}$ are phase functions which arise due to pericenter precession. Note that here one must incorporate the evolution in the eccentricity by solving Eqs. (10–11), i.e. $\dot\nu \equiv \dot\nu(\nu) = \dot\nu[\nu, e(\nu)]$, and similarly for $\dot\gamma$ (see Eq. (36) below).

III. FOURIER TRANSFORMATION OF THE ECCENTRIC INSPIRAL WAVEFORM

The sensitivity of a GW detector is usually given in Fourier-space. Thus, to estimate the detection signal to noise ratio and measurement accuracy, we construct the Fourier transform of the waveform as

$$h(f) = \int_{-\infty}^{\infty} \widetilde{h}(t) e^{2\pi i t f} dt \,, \tag{14}$$

where f is the Fourier frequency. These integrals cannot be evaluated analytically without further assumptions. However, since the orbital parameters (a, e) evolve very slowly relative to the GW phase, the stationary phase approximation (SPA) can be utilized [62] (Appendix B). We account for the adiabatic time evolution during the inspiral in the Fourier-transformed waveform $h(f)$ using Eqs. (12–13) and the SPA. In this approximation the Fourier transformation of the waveform becomes a discrete sum over the harmonics of orbital frequency, $f_n = n\nu$. When the pericenter precession is taken into account, each harmonic f_n, is split into a triplet $\mathbf{f} \equiv (f_n, f_{n\pm})$ and therefore the waveform consists of the sum over these triplets of Fourier frequencies:

$$\begin{aligned} h_\times(\mathbf{f}) = &-\frac{h_0}{2}\sum_n \cos\Theta\Big[B_n^- \Lambda_+ e^{i(\Psi_{n+}+\pi/4)} \\ &+ B_n^+ \Lambda_- e^{i(\Psi_{n-}+\pi/4)}\Big] \,, \end{aligned} \tag{15}$$

$$\begin{aligned} h_+(\mathbf{f}) = &-\frac{h_0}{4}\sum_n \Big[\sin^2\Theta A_n \Lambda e^{i(\Psi_n - \pi/4)} \\ &+ \left(1+\cos^2\Theta\right)\Big(B_n^+ \Lambda_- e^{i(\Psi_{n-}-\pi/4)} \\ &- B_n^- \Lambda_+ e^{i(\Psi_{n+}-\pi/4)}\Big)\Big] \,, \end{aligned} \tag{16}$$

where $f_n = n\nu$, $f_{n\pm} = n\nu \pm \frac{\dot\gamma}{\pi}$; $h_0 = 4\mathcal{M}^{5/3}\left(2\pi\nu\right)^{2/3}/D_L$ is the amplitude corresponding to the orbital frequency; $\Psi_n = 2\pi f t_n - \Phi_n$, $\Psi_{n\pm} = 2\pi f t_{n\pm} - \Phi_{n\pm}$ are phase functions (where t_n, $t_{n\pm}$ are the time parameters of the SPA, see Appendix B). We have introduced the notation $\Lambda_\pm = (n\dot\nu \pm \ddot\gamma/\pi)^{-1/2}$ and $\Lambda = (n\dot\nu)^{-1/2}$. The phases Ψ_n and $\Psi_{n\pm}$ depend on the corresponding Fourier frequencies f_n, $f_{n\pm}$, respectively.

We recall that for circular orbits (i.e. $e \to 0$) the waveforms in Eqs. (15) and (16) simplify as

$$h_\times^\circ(f) = -2\sqrt{\frac{5}{96}}\frac{\mathcal{M}^{5/6} f^{-7/6}}{\pi^{2/3} D_L}\cos\Theta e^{i\Psi_\circ^+} \,, \tag{17}$$

$$h_+^\circ(f) = -\sqrt{\frac{5}{96}}\frac{\mathcal{M}^{5/6} f^{-7/6}}{\pi^{2/3} D_L}\left(1+\cos^2\Theta\right) e^{i\Psi_\circ^-} \,, \tag{18}$$

where $f = 2\nu$ is the (circular) Fourier frequency and $\Psi_\circ^\pm = 2\pi f t_c - \Phi_c \pm \pi/4 + (3/4)\left(8\pi\mathcal{M}f\right)^{-5/3}$ is the well-known phase function.

A. LISA detector response

With its three arms LISA represents a pair of two orthogonal arm detectors, I and II, producing two linearly independent signals. The frequency domain waveforms are

$$h^{I,II}(\mathbf{f}) = \frac{\sqrt{3}}{2}\left[F_\times^{I,II} h_\times(\mathbf{f}) + F_+^{I,II} h_+(\mathbf{f})\right] \,, \tag{19}$$

with the antenna-beam pattern functions

$$F_\times^I = \tfrac{1+\mu_S^2}{2}\cos 2\phi_S \sin 2\psi_S + \mu_S \sin 2\phi_S \cos 2\psi_S \,, \tag{20}$$

$$F_+^I = \tfrac{1+\mu_S^2}{2}\cos 2\phi_S \cos 2\psi_S - \mu_S \sin 2\phi_S \sin 2\psi_S \,, \tag{21}$$

where $\mu_{S,L} = \cos\theta_{S,L}$ with (θ_S, ϕ_S) being spherical angels of the source in the detector-based coordinate system. The angle ψ_S is the polarization angle that can be expressed by the position of the detector and the orbital plane [8]. The other antenna-beam pattern functions are $F^{II}_{+,\times} = F^{I}_{+,\times}(\phi_S - \pi/4)$. The quantities θ_S, ϕ_S and ψ_S are time dependent because the LISA constellation moves around the Sun and these explicit time evolutions are [8]

$$\mu_S = \frac{\bar{\mu}_S}{2} - \frac{\sqrt{3}\bar{\lambda}_S}{2}\cos\bar{\phi}^t_S \ , \tag{22}$$

$$\phi_S = \alpha_1(t) + \frac{\pi}{12} + \arctan\frac{\sqrt{3}\bar{\mu}_S + \bar{\lambda}_S\cos\bar{\phi}^t_S}{2\bar{\lambda}_S\sin\bar{\phi}^t_S} \ , \tag{23}$$

$$\psi_S = \arctan\frac{\bar{\mu}_L - \sqrt{3}\bar{\lambda}_L\cos\bar{\phi}^t_L - \cos\Theta\left(\bar{\mu}_S - \sqrt{3}\bar{\lambda}_S\cos\bar{\phi}^t_S\right)}{2K} \tag{24}$$

where $\bar{\lambda}_{S,L} = \sin\bar{\theta}_{S,L}$, $\bar{\mu}_{S,L} = \cos\bar{\theta}_{S,L}$ and $\bar{\phi}^t_{S,L} = \bar{\phi}(t) - \bar{\phi}_{S,L}$, with $\bar{\theta}_S$, $\bar{\phi}_S$ being the spherical angles of the source's position. The angles $\bar{\theta}_L$, $\bar{\phi}_L$ correspond to the direction of orbital angular momentum in the barycenter frame [8]. In Eqs. (22-24) $\Theta = \arccos\left[\bar{\mu}_L\bar{\mu}_S + \bar{\lambda}_L\bar{\lambda}_S\cos(\bar{\phi}_L - \bar{\phi}_S)\right]$ is the inclination (in Eqs. (3), (4)) and the explicit time dependence are $\alpha_1(t) = 2\pi t/T - \pi/12 + \alpha_0$, $\bar{\phi}(t) = \bar{\phi}_0 + 2\pi t/T$, and

$$\begin{aligned} K = &\frac{\bar{\lambda}_L\bar{\lambda}_S}{2}\sin(\bar{\phi}_L - \bar{\phi}_S) \\ &- \frac{\sqrt{3}}{2}\cos\bar{\phi}(t)\left(\bar{\mu}_L\lambda_S\sin\bar{\phi}_S - \bar{\mu}_S\bar{\lambda}_L\sin\bar{\phi}_L\right) \\ &- \frac{\sqrt{3}}{2}\sin\bar{\phi}(t)\left(\bar{\mu}_S\bar{\lambda}_L\cos\bar{\phi}_L - \bar{\mu}_L\bar{\lambda}_S\cos\bar{\phi}_S\right) . \end{aligned} \tag{25}$$

We note that $\bar{\theta}_L$, $\bar{\phi}_L$ are generally not constants for spinning binaries due to spin-orbit effects, but we neglect these effects here.

We carry out the analysis for the single-detector case (I only) and the full two-detector configuration ($I + II$).

In practice, the measured signal in Eq. (19) is truncated at a minimum and maximum frequency corresponding to the start of the observation and the last stable orbit for each harmonic, respectively (see Sec. V. A. below).

IV. PARAMETER ESTIMATION

In this section we review the basics of Bayesian parameter estimation. The measured signal $\widetilde{s}(t)$ is made up of the GW $\widetilde{h}(t)$ and the noise $\widetilde{n}(t)$

$$\widetilde{s}(t) = \widetilde{h}(t) + \widetilde{n}(t) \ . \tag{26}$$

We assume that the noise is stationary, Gaussian, and statistically independent at different frequencies. Then each Fourier component has a Gaussian probability distribution and the different Fourier components of the noise are "uncorrelated", i.e.,

$$p(n = n_0) \propto e^{-(n_0|n_0)^2} \ , \tag{27}$$

$$\langle n(f)n^*(f')\rangle = \frac{1}{2}\delta(f - f')S(f) \ . \tag{28}$$

In Eqs. (27), (28) $p(n)$ is the probability for the noise, the inner product is defined by

$$(g \mid k) = 4\Re\int_0^\infty \frac{g(f)k^*(f)}{S(f)}df \ , \tag{29}$$

the k^* is denotes complex conjugation and $S(f)$ is the one sided spectral noise density. The definition of the signal-to-noise ratio (SNR) of h is

$$\rho^2 = (h \mid h) = 4\Re\int_0^\infty \frac{h(f)h^*(f)}{S(f)}df \ . \tag{30}$$

The waveform $h(f)$ depends on the parameters λ^a which characterize the source. For large SNR, the errors $\Delta\lambda^a$ have the Gaussian probability distribution

$$p(\Delta\lambda^c) = p_0 e^{-\Gamma_{ab}\Delta\lambda^a\Delta\lambda^b/2} \ . \tag{31}$$

where p_0 is the normalization factor and Γ_{ab} is the Fisher information matrix defined by

$$\mathbf{\Gamma}_{ab} = (\partial_a h \mid \partial_b h) = 4\Re\int_0^\infty \frac{\partial_a h(f)\partial_b h^*(f)}{S(f)}df \ , \tag{32}$$

with $\partial_a = \partial/\partial\lambda^a$. The inverse of the Fisher matrix is approximately the Σ_{ab} variance-covariance matrix for $\rho \gg 1$, which gives the accuracy of each parameter and defined by $\Sigma_{ab} = (\Gamma_{ab})^{-1} = \left\langle\Delta\lambda^a\Delta\lambda^b\right\rangle$. The root-mean-square errors of the parameters λ^a are $\Delta\lambda^a = \sqrt{\mathbf{\Sigma}_{aa}}$.

For example, the error of the sky position solid angle is

$$\Delta\Omega_S = 2\pi\sqrt{\left(\Delta\overline{\mu}_S\Delta\overline{\phi}_S\right)^2 - \left\langle\Delta\overline{\mu}_S\Delta\overline{\phi}_S\right\rangle^2} \ . \tag{33}$$

The source localization sky area is an ellipse with semiminor and major axes (a_S, b_S) given by Eq. (4.12) in Ref. [11]. The SNR and Fisher matrix for the LISA configuration are

$$\begin{aligned} \rho^2 &= \rho^2_I + \rho^2_{II} \ , \\ \mathbf{\Gamma}_{ab} &= \mathbf{\Gamma}^I_{ab} + \mathbf{\Gamma}^{II}_{ab} \ . \end{aligned} \tag{34}$$

where the I, II subscripts distinguish the h^I, h^{II} waveforms in Eq. (19).

V. MEASURING ECCENTRIC INSPIRALING SMBH BINARIES

We focus on comparable–mass SMBH binaries in the range $(10^4 - 10^7)M_\odot$ which correspond to the measured frequency range $\left(10^{-4} - 10^{-1}\right)$ Hz. For initial configurations one year before merger, we assume that the binary has e_0 orbital eccentricity and γ_0 pericenter position. The 10-dimensional parameter space is

$$\lambda^a = \{\ln D_L, \ln\mathcal{M}, t_c, \Phi_c, \bar{\phi}_S, \bar{\mu}_S, \bar{\phi}_L, \bar{\mu}_L, e_0, \gamma_0\}$$

In the circular case e_0 and γ_0 do not appear. Note that only one mass parameter, the chirp mass $\mathcal{M}$ enters the leading-order waveform. Our assumptions are:

- To examine the effects of eccentricity and pericenter precession, we neglect higher order post-Newtonian (beyond 1PN orders and spins), we only use the *heuristic* pericenter precession in phase described above.

- In all cases take $t_c = \Phi_c = \gamma_0 = 0$ (we use the $\alpha_0, \bar{\phi}_0 = 0$ choice, as in [8]).

- We assume that the observation time is one year before the merger, more precisely, before the *Newtonian last stable orbit* (LSO) which is defined by [54]

$$\nu^N_{LSO} = \frac{1}{2\pi m}\left(\frac{1-e^2_{LSO}}{6+2e_{LSO}}\right)^{3/2} \;, \tag{35}$$

  where e_{LSO} is the final eccentricity at the last stable orbit ($\nu(e_{LSO}) = \nu_{LSO}$).

- For the $n^{\rm th}$ orbital harmonic, the limits of integration are taken to be $\nu_{\max} = \nu_{LSO}$ and $\nu_{\min} = \max\{\nu_0, f_c/n\}$ where ν_0 is the frequency one-year before the LSO and $f_c = 0.03\,\text{mHz}$ is the cut-off frequency of the LISA detector.

- We assume that luminosity distance to the source is $D_L = 6.4\,\text{Gpc}$ corresponding to a cosmological redshift $z = 1$, and use the comoving masses as free parameters, $m^z_i = (1+z)m_i$ [9]. We do not take into account the Doppler phase due to the varying light travel during the LISA orbit around the Sun.

- We parametrize the evolution of the orbital frequency with the instantaneous eccentricity following [38] (Appendix A).

$$\nu(e) = \nu_0\frac{\sigma(e)}{\sigma(e_0)} \tag{36}$$

  where ν_0 and e_0 are the initial orbital frequency and eccentricity and $\sigma(e)$ follows from Ref. [21].

- We truncate the harmonics at $n_{\max}$ where 99% of the signal power corresponds to [38]

$$n_{\max} = \left| 5\frac{(1+e_0)^{1/2}}{(1-e_0)^{3/2}} \right| \;. \tag{37}$$

  Here $n_{\max} = \{9, 24\}$ for $e_0 = \{0.3, 0.6\}$, respectively.

- We analyzed 10^4 SMBH binaries where the angular variables were chosen randomly, i.e. for $\bar{\phi}_S$, $\bar{\phi}_L$ in the range $(0, 2\pi)$ and for $\bar{\theta}_S$, $\bar{\theta}_L$ in the range $(-\pi/2, \pi/2)$.

The computation of SNR and the Fisher matrix with the above general definition Eq. (14) is numerically expensive for a large set of binaries. We resort to the SPA waveform. The SNR and the Fisher information matrix consist of three terms for each orbital harmonic which correspond to $(f_n,\, f_{n\pm})$, respectively,

$$\hat{\rho}^2 = \sum_n \left(\hat{\rho}^2_n + \hat{\rho}^2_{n+} + \hat{\rho}^2_{n-}\right) \tag{38}$$

$$\hat{\mathbf{\Gamma}}_{ab} = \sum_n \left(\hat{\mathbf{\Gamma}}^n_{ab} + \hat{\mathbf{\Gamma}}^{n+}_{ab} + \hat{\mathbf{\Gamma}}^{n-}_{ab}\right) \tag{39}$$

where we have introduced the notations $\hat{\rho}^2_{n,n+,n-} = (h_{n,n+,n-} \mid h_{n,n+,n-})$, $\hat{\mathbf{\Gamma}}^{n,n+,n-}_{ab} = (\partial_a h_{n,n+,n-} \mid \partial_b h_{n,n+,n-})$ and $h_{n,n+,n-} = h(f_{n,n+,n-})$. Here we neglect the cross terms between different harmonics n, $n+$, and $n-$, in $\hat{\rho}$ and $\hat{\mathbf{\Gamma}}_{ab}$. We used the LISA sensitivity curve generator [65]. In the SPA, we can change integration variables from f_n ,$f_{n\pm}$ to e.

$$\hat{\rho}^2_n = 4\Re\int_{e_{\min}}^{e_{\max}} \frac{h_n(e)h^*_n(e)}{S\left[n\nu(e)\right]}\frac{nd\nu}{de}de \;, \tag{40}$$

$$\hat{\mathbf{\Gamma}}^n_{ab} = 4\Re\int_{e_{\min}}^{e_{\max}} \frac{\partial_a h_n(e)\partial_b h^*_n(e)}{S\left[n\nu(e)\right]}\frac{nd\nu}{de}de \;, \tag{41}$$

where $d\nu/de$ and $\nu(e)$ are given by Eqs. (A1), (A3) and $e_{\max} = e_{LSO}$, $e_{\min} = \min\{e_c(n), e_0\}$ (here $e_c(n)$ corresponds to f_c/n where $f_c = 0.03mHz$ is the cut-off frequency for the LISA detector).

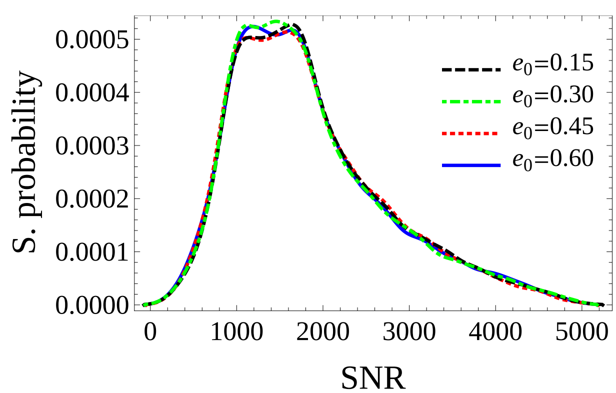

FIG. 2. (color online) Smooth probability density function of SNR for various initial eccentricities $e_0 = 0.15, 0.3, 0.45, 0.6$ and masses $\left(10^6 - 10^6\right) M_\odot$. The eccentricity dependence of SNR is almost negligible.

VI. RESULTS AND DISCUSSION

We find that the LISA parameter estimation accuracy depends sensitively on the initial eccentricity and pericenter precession and we also examined the distribution of parameter errors for a wide range of initial binary parameters and masses. The four angular parameters

TABLE I. The initial and final frequencies (ν_0 and $\nu_1 = \nu_{LSO}$) for various initial eccentricities (e_0) and comoving masses (m_1–m_2 and redshift is $z = 1$) for a one-year inspiral before LSO We used the shorthand notation $e_1 = e_{LSO}$ for the final eccentricity. We have completed with dimensionless semimajor axis $\bar{r} = a/m$ at initial ($\bar{r_0}$) and final points ($\bar{r_1}$).

$SMBH\ [M_\odot]$	$e_0 = 0$	$e_0 = 0.3$	$e_0 = 0.6$
$10^7 - 10^7$	$\nu_0 = 3.47\mu$Hz, $\bar{r}_0 = 37.84$ $\nu_1 = 54.96\mu$Hz, $\bar{r}_1 = 6.00$	$\nu_0 = 3.05\mu$Hz, $\bar{r}_0 = 41.21$ $\nu_1 = 54.47\mu$Hz, $\bar{r}_1 = 6.04$ $e_1 = 0.017$	$\nu_0 = 1.92\mu$Hz, $\bar{r}_0 = 56.17$ $\nu_1 = 53.78\mu$Hz, $\bar{r}_1 = 6.09$ $e_1 = 0.039$
$10^6 - 10^6$	$\nu_0 = 14.64\mu$Hz, $\bar{r}_0 = 67.23$ $\nu_1 = 549.59\mu$Hz, $\bar{r}_1 = 6.00$	$\nu_0 = 12.88\mu$Hz, $\bar{r}_0 = 73.28$ $\nu_1 = 547.75\mu$Hz, $\bar{r}_1 = 6.01$ $e_1 = 0.007$	$\nu_0 = 8.09\mu$Hz, $\bar{r}_0 = 99.87$ $\nu_1 = 545.22\mu$Hz, $\bar{r}_1 = 6.03$ $e_1 = 0.015$
$10^5 - 10^5$	$\nu_0 = 61.73\mu$Hz, $\bar{r}_0 = 119.64$ $\nu_1 = 5495.90\mu$Hz, $\bar{r}_1 = 6.00$	$\nu_0 = 54.31\mu$Hz, $\bar{r}_0 = 130.30$ $\nu_1 = 5488.93\mu$Hz, $\bar{r}_1 = 6.01$ $e_1 = 0.003$	$\nu_0 = 34.13\mu$Hz, $\bar{r}_0 = 177.59$ $\nu_1 = 5479.18\mu$Hz, $\bar{r}_1 = 6.01$ $e_1 = 0.006$
$10^4 - 10^4$	$\nu_0 = 260.30\mu$Hz, $\bar{r}_0 = 212.75$ $\nu_1 = 54959\mu$Hz, $\bar{r}_1 = 6.00$	$\nu_0 = 229.02\mu$Hz, $\bar{r}_0 = 231.72$ $\nu_1 = 54934\mu$Hz, $\bar{r}_1 = 6.00$ $e_1 = 0.001$	$\nu_0 = 143.94\mu$Hz, $\bar{r}_0 = 315.80$ $\nu_1 = 54896\mu$Hz, $\bar{r}_1 = 6.01$ $e_1 = 0.002$

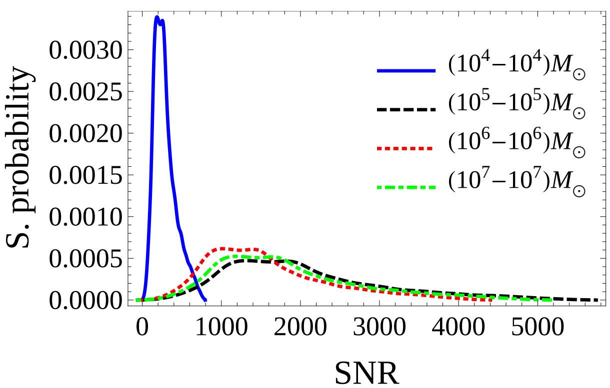

FIG. 3. (color online) Smooth probability density function of SNR for various equal-mass binaries (for initial eccentricities $e_0 = 0.3$). The SNR is $\mathcal{O}(10^2)$ order for low-mass binaries $\left(10^4 - 10^4\right) M_\odot$. In the other cases the SNR is $\mathcal{O}(10^3)$ order

$(\bar{\phi}_S, \bar{\mu}_S, \bar{\phi}_L, \bar{\mu}_L)$ are chosen randomly in a Monte Carlo sampling, and the cosmological redshift and luminosity distance are fixed at $z = 1$ and $D_L = 6.4$Gpc. Figures 5-10 show the histograms of the expected measurement errors of the binary parameters for the chirp mass $\Delta\mathcal{M}/\mathcal{M}$, initial eccentricity Δe_0, and angular resolution $\Delta\Omega_S$ for equal-mass binaries with 10^6 or $10^7 M_\odot$ each. Our parametrization of the orbit is singular at $e_0 = 0$. To get around this, we use $e_0 = 10^{-6}$ for circular orbits. We have presented three representative cases for the initial eccentricity: a nearly *circular* orbit with $e_0 = 10^{-6}$ (see Table II and Fig. 4), and orbits with *medium* $e_0 = 0.3$ and *high* $e_0 = 0.6$ eccentricities. Our computations correspond to a one-year inspiral before LSO. The initial and final orbital frequencies (ν_0 and ν_{LSO}) vary for the three kinds of initial eccentricities and different equal-mass SMBH binaries as shown in Table I. If increasing initial eccentricity e_0, the initial frequency ν_0 decreases one year before LSO, while the final frequency ν_{LSO} does not change significantly due to the fact that e_{LSO} is close to zero.

Representative values are shown in Table II for equal-mass SMBHs for a fixed set of angular configurations ($\bar{\phi}_S = 4.642$, $\bar{\mu}_S = -0.3185$, $\bar{\phi}_L = 4.724$ and $\bar{\mu}_L = -0.3455$). The table shows that accounting for the eccentricity in the waveform improves some of the parameter errors such as the errors of the angular resolution $\Delta\Omega_S$, initial eccentricity Δe_0 and the chirp mass $\Delta\mathcal{M}/\mathcal{M}$ for higher-mass SMBH binaries $(10^6 - 10^7)M_\odot$. For lower masses, i.e. $(10^4 - 10^5)M_\odot$, the eccentricity and precession have no essential effects on parameter estimation. For masses $10^4 M_\odot$ the high eccentricity has no significant effect on the parameters $\Delta\mathcal{M}/\mathcal{M}$ and $\Delta\Omega_S$. However, the initial eccentricity errors (Δe_0) are improved for smaller masses typically by factors of 3–10 and they are greatly improved for larger initial eccentricities by orders of magnitude. Similarly, the source localization angular resolution $\Delta\Omega_S$ decreases with increasing eccentricity and masses. However, pericenter precession does improve the parameter errors for higher-mass SMBHs. It can be seen that the eccentricity, compared to the circular orbit case, does improve the error of luminosity distance $\Delta D_L/D_L$, but there is no essential change between the high and medium eccentricities and the inclusion of the pericenter precession. The error of t_c is not affected by the eccentricity and pericenter precession. It is interesting to note that there are degeneracies ($\Delta\Phi_c, \Delta\gamma_0 > 1$) for errors of Φ_c and γ_0 in the nearly circular case, which can be explained by the fact that our parametrization of the orbit is singular at $e_0 = 0$. For eccentric orbits

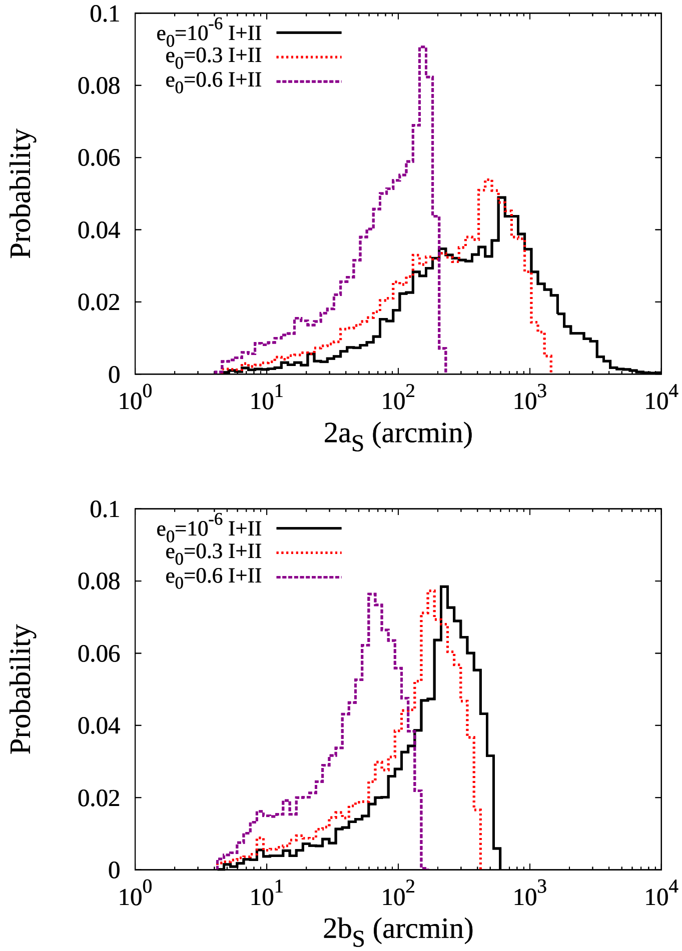

FIG. 4. (color online) Distribution of the major (top) and minor (bottom) axes (a_S, b_S) of the sky position error ellipse $(\Delta\Omega_S = \pi a_S b_S)$ for various eccentric binaries with equal mass (here the pericenter precession is neglected). The two panels correspond to 1-year observation of $\left(10^7 - 10^7\right) M_\odot$ black hole binaries at $z = 1$ ($D_L = 6.4$Gpc) with LISA (2 detector). The angular resolution is improved for high-mass binaries.

(medium and high initial eccentricities) this degeneracy disappears (the errors of t_c, Φ_c and γ_0 are not presented in Table II).

Figures 2 and 3 show the distribution of the SNR for different binary orientations, for various eccentricities and masses. The SNR is similar for equal-mass binaries with $10^5 M_\odot \leq M \leq 10^7 M_\odot$, but significantly smaller for $10^4 M_\odot$ SMBH or less. Remarkably, the SNR does not change significantly with the initial eccentricity, which is consistent with previous studies for small eccentricities [55]. This shows that the systematic improvement of the parameter estimation accuracy for eccentric sources is due to the breaking of correlations between different parameter errors instead of an overall change in the SNR.

Figures 4 shows the distribution of the major/minor axes of the sky position error ellipse for the nearly circular, medium and high initial eccentricity orbits. The shape of the error ellipse is important in coordinating GW observations with telescopes [11, 19]. It can be seen that the error of the major/minor axes is improved for highly eccentric binaries.

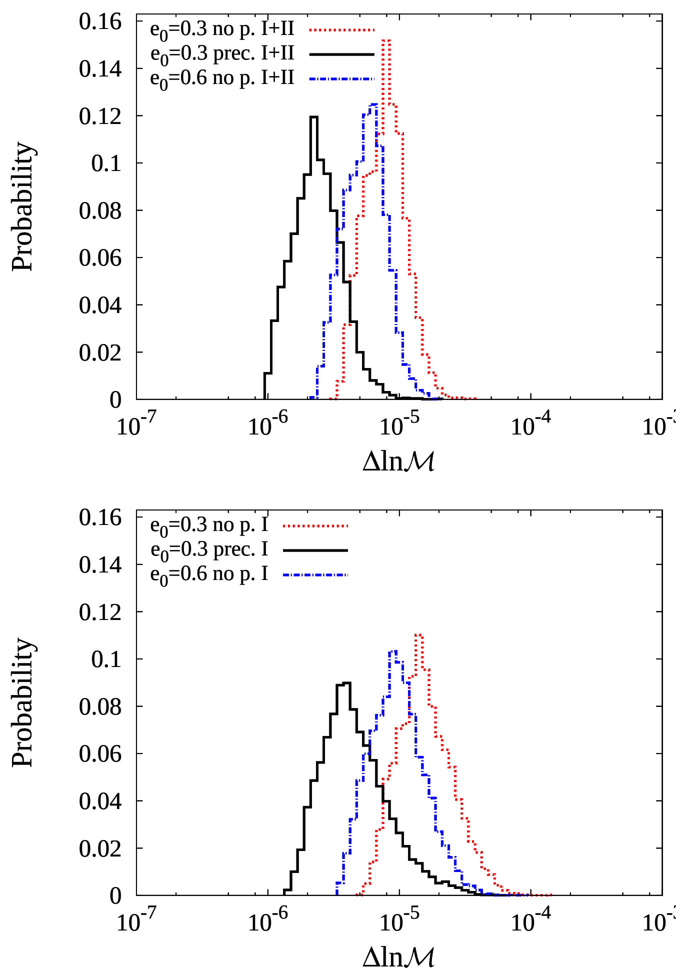

FIG. 5. (color online) Estimated distribution of the chirp mass errors in the precessing and non-precessing cases for the total $(I + II$, top) and single (I, bottom) detectors. The results are shown for medium ($e_0 = 0.3$) and high ($e_0 = 0.6$) initial eccentricities and higher-mass SMBH binaries $\left(10^6 - 10^6\right) M_\odot$. For precessing sources the $e_0 = 0.6$ case is omitted in both figures due to the high degree overlap with the $e_0 = 0.3$ case.

Figures 5 and 6 show that the chirp mass errors are greatly improved for a larger initial eccentricity for $10^6 M_\odot$ and $10^7 M_\odot$ equal-mass SMBH binaries (see also [13]). Furthermore, the chirp mass measurement errors are improved by an additional factor 2–5 due to pericenter precession for relatively massive $10^7 M_\odot$ binaries, but not for $10^6 M_\odot$ binaries. The typical chirp mass error is about 10^{-5} for $10^7 M_\odot$, and 10^{-4} for $10^6 M_\odot$ binaries.

Figures 7 and 8 show that the initial eccentricity errors

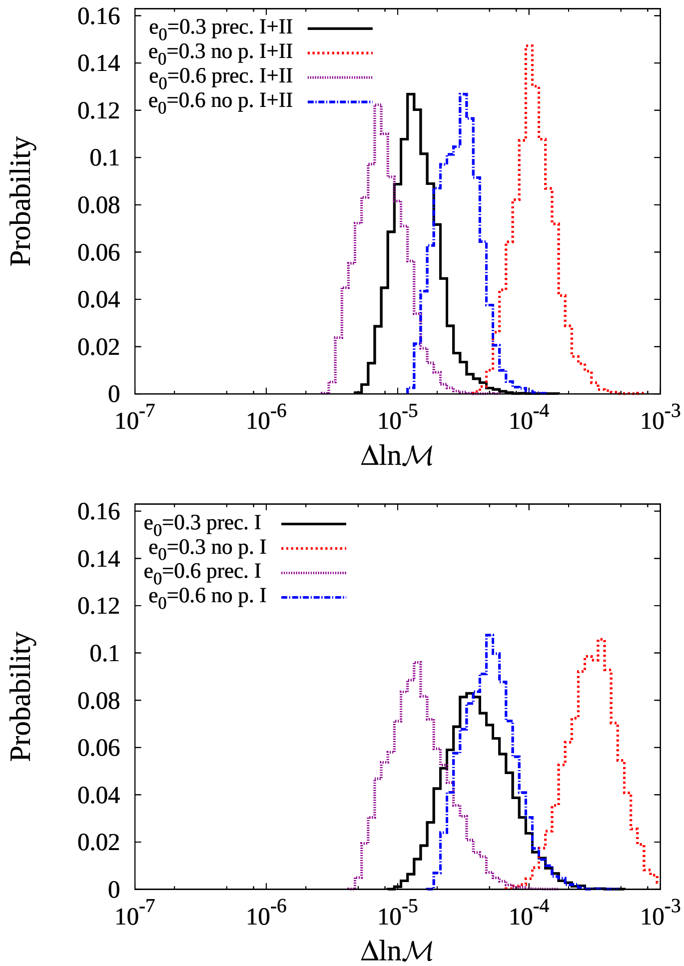

FIG. 6. (color online) Same as Fig. 5 but for masses $(10^7 - 10^7)\,M_\odot$.

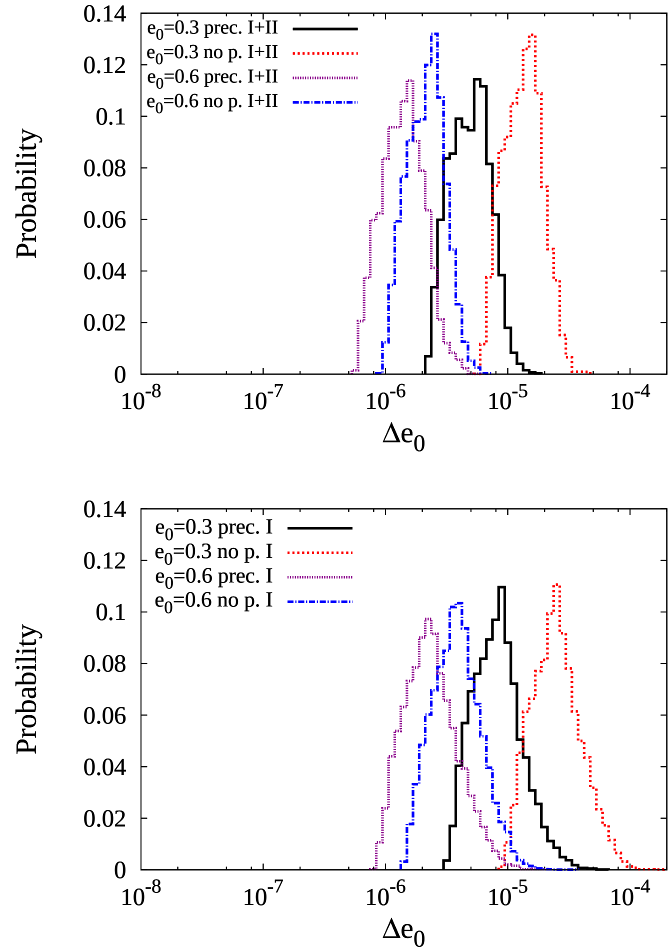

FIG. 7. (color online) Estimated distribution of the initial eccentricity errors in the precessing and non-precessing cases for the total ($I + II$, top) and single (I, bottom) detectors. The results are shown for medium ($e_0 = 0.3$) and high ($e_0 = 0.6$) initial eccentricities and higher-mass SMBH binaries $(10^6 - 10^6)\,M_\odot$.

are also improved for a high eccentricity, the initial eccentricity parameter can be measured with high accuracy; Δe_0 is about $10^{-5} - 10^{-4}$ for $10^7 M_\odot$, and $10^{-4} - 10^{-3}$ for $10^6 M_\odot$ binaries. Pericenter precession improves the eccentricity errors by a factor of 10 for $10^7 M_\odot$ and by a factor 2–3 for $10^6 M_\odot$.

Figure 9 and 10 show that the typical source sky localization accuracy for equal-mass binaries for binaries at $z = 1$ ranges between $10^{-4} - 10^{-2}$ steradians. Consistent with previous studies [12, 13], we find that the errors improve for higher initial eccentricities ($e_0 = 0.6$), compared to the cases of moderate to small initial eccentricities ($e_0 = 0.3$) for equal-mass $10^7 M_\odot$ binaries. The error $\Delta\Omega_S$ in the total two-detector case is about one order of magnitude better than for a single detector [8]. For high initial eccentricities, the angular resolution of the total detector case is improved more compared to the single detector case for $10^7 M_\odot$ binaries (see Fig.10). In contrast to the chirp mass and the eccentricity errors, the angular localization capabilities are not improved for eccentric equal-mass $10^6 M_\odot$ binaries but they are improved for $10^7 M_\odot$ binaries. Figure 9 and 10 clearly show that pericenter precession does not affect the sky position error for either mass choice.

A possible explanation for the qualitatively different improvement of the sky position and mass-eccentricity errors is that the sky position is a slow parameter, as opposed to fast parameters like the chirp mass and eccentricity [18]. The slow parameters are determined by the slow orbital modulation of the signal by the detector's motion around the Sun while the fast parameters also depend on the orbital phase. The correlations between the slow parameters become large during the last week before merger when the signal-to-noise ratio increases, which prohibits the rapid improvement of the slow parameters' marginalized errors. Pericenter precession does not vary

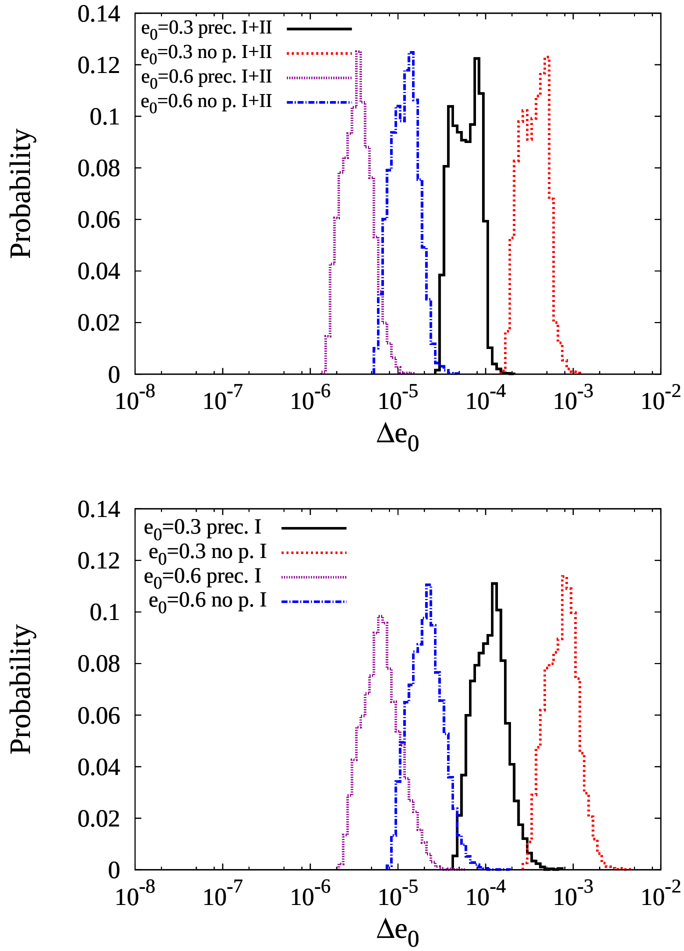

FIG. 8. (color online) Same as Fig. 7 but for masses $\left(10^7 - 10^7\right) M_\odot$.

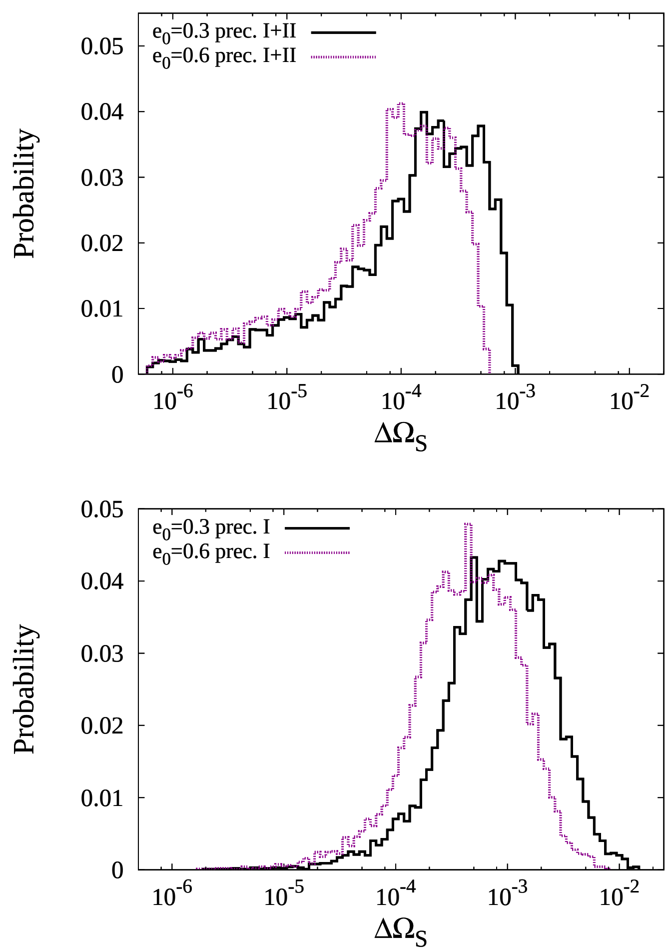

FIG. 9. (color online) Estimated distribution of the angular resolution $\Delta\Omega_S$ in the precessing case for the total $(I + II$, top) and single $(I$, bottom) detectors. The results are shown for medium $(e_0 = 0.3)$ and high $(e_0 = 0.6)$ initial eccentricities and higher-mass SMBH binaries $\left(10^6 - 10^6\right) M_\odot$. The curves for the non-precessing $e_0 = 0.3$ and $e_0 = 0.6$ cases are omitted in both figures since they are close and very similar to the curves for the precessing ones.

the binary inclination, and cannot effectively break the correlation between slow parameters. However, pericenter precession splits the GW frequency into a triplet for each harmonic which can break degeneracies for the fast parameters and efficiently improve their measurement errors.

VII. CONCLUSIONS

We carried out an extensive study of parameter estimation for eccentric binaries with arbitrary orbital eccentricity. We computed the waveforms in frequency domain by a new method optimized for taking into account eccentricity, by changing the integration variable for the waveforms from the orbital frequency $\nu(e)$ to the eccentricity variable e [38]. This results in an improvement of numerical precision as compared to standard approaches in frequency domain, where a Taylor series expansion of the orbital frequency $\nu(e)$ (among others) in the eccentricity e is needed [55]. Our method is well suited for computing the Fisher matrix and the signal-to-noise ratio. Our parameter space is 10 dimensional, consisting of 4 angles, the chirp mass, the luminosity distance, coalescence time and phase, initial eccentricity and pericenter position (compare Fig. 1). The first 8 parameters are standard for circular orbits too.

We have examined the LISA parameter estimation errors for GWs emitted by eccentric inspiraling SMBH binaries including the effects of pericenter precession. Based on a large set of simulated binary waveforms, we found that there is about one order of magnitude improvement compared to circular waveforms in LISA's angular resolution for highly eccentric sources (e.g. $e_0 =$

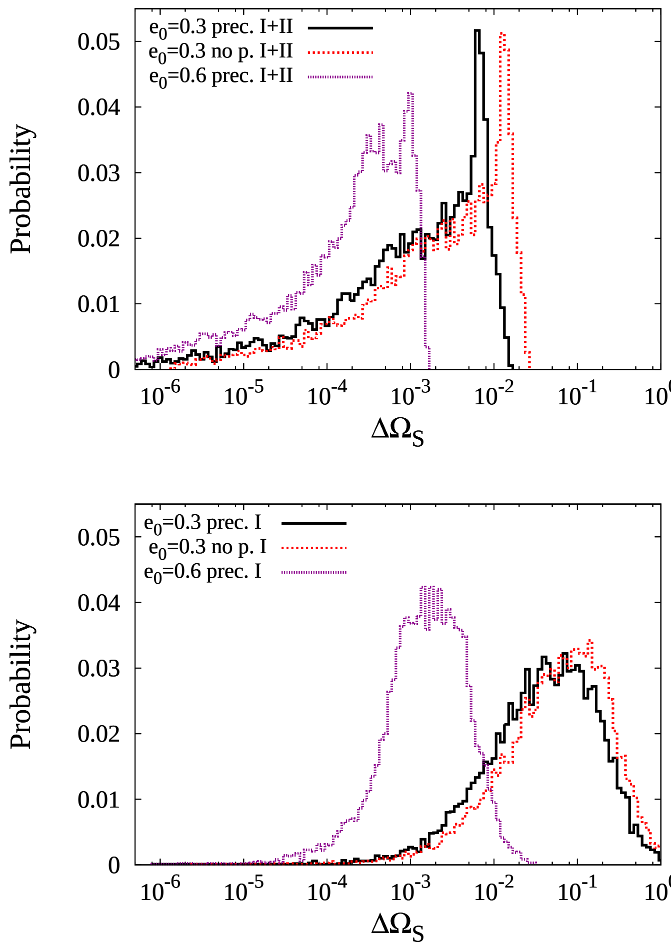

FIG. 10. (color online) Estimated distribution of the angular resolution $\Delta\Omega_S$ in the precessing and non-precessing cases for the total ($I+II$, top) and single (I, bottom) detectors. The results are shown for medium ($e_0 = 0.3$) and high ($e_0 = 0.6$) initial eccentricities and higher-mass SMBH binaries $\left(10^7 - 10^7\right) M_\odot$. For non-precessing sources the $e_0 = 0.6$ case is omitted in both figures since it is close and very similar to the curve for the $e_0 = 0.6$ precessing case.

0.6) for relatively high SMBH masses $\sim 10^7 M_\odot$. There is however, a much smaller effect for lower mass binaries in the range $(10^4 - 10^5) M_\odot$. This improves the prospects for identifying the electromagnetic counterparts [17, 19] of relatively high mass eccentric SMBH mergers with LISA. Similar conclusions have been reached in Refs. [12, 13]. However, we found that pericenter precession does not further improve the sky localization accuracy of the source, although it may further improve the measurement errors of mass and eccentricity parameters.

It is important to note that the angular resolution is significantly affected by the number of detectors, see Figs. 9–10. However, nearly the same parameter estimation accuracy can be obtained for the single and total detector configurations for $(10^6 - 10^6) M_\odot$ binaries for fast parameters [18] like the chirp mass and eccentricity (Figs. 5 and 7). The second detector systematically reduces the errors of these parameters for higher masses $(10^7 - 10^7) M_\odot$.

ACKNOWLEDGMENTS

We thank László Godán for carefully reading the manuscript and for useful discussions. This work was supported by the Hungarian Scientific Research Fund (OTKA) grants NI68228, K101709. BK acknowledges support from NASA through Einstein Postdoctoral Fellowship Award Number PF9-00063 issued by the Chandra X-ray Observatory Center, which is operated by the Smithsonian Astrophysical Observatory for and on behalf of the National Aeronautics Space Administration under contract NAS8-03060.

Appendix A: Orbital evolution and waveform

According to Eqs. (10) and (11), the equation

$$\frac{d\nu}{de} = -\frac{18\nu}{19} \frac{1 + \frac{73}{24}e^2 + \frac{37}{96}e^4}{e(1-e^2)\left(1 + \frac{121}{304}e^2\right)} , \tag{A1}$$

can be solved as

$$\nu(e) = C_0 e^{-18/19} \left(1 - e^2\right)^{3/2} \left(1 + \frac{121}{304}e^2\right)^{-1305/2299} , \tag{A2}$$

where $C_0 = \nu_0 e_0^{18/19} \left(1 + \frac{121}{304}e_0^2\right)^{1305/2299} \left(1 - e_0^2\right)^{-3/2}$ is the integration constant that has been chosen to set the initial condition $\nu(e_0) = \nu_0$ for the initial values e_0 and ν_0. Then Eq. (A2) is

$$\nu(e) = \nu_0 \frac{\sigma(e)}{\sigma(e_0)} , \tag{A3}$$

where $\sigma(e) = e^{-18/19} \left(1 - e^2\right)^{3/2} \left(1 + \frac{121}{304}e^2\right)^{-1305/2299}$. From Eqs. (10) and (11) one can compute the evolution of the time and phase functions ($t - t_c = \int_0^e \frac{de'}{\dot{e}(e')}$, $\Phi - \Phi_c = 2\pi \int_0^e \frac{\nu(e')}{\dot{e}(e')} de$) in terms of eccentricity as, see Eqs. (11) and (A3),

$$t - t_c = -\frac{15}{304\mathcal{M}^{5/3}} \left(\frac{\sigma(e_0)}{2\pi\nu_0}\right)^{8/3} I_t(e) \tag{A4}$$

$$\Phi - \Phi_c = -\frac{15}{304\mathcal{M}^{5/3}} \left(\frac{\sigma(e_0)}{2\pi\nu_0}\right)^{5/3} I_\phi(e) , \tag{A5}$$

where the I_t and I_ϕ integrals are

$$I_t(e) = \int_0^e \frac{x^\alpha \left(1 - \delta x^2\right)^{-\beta}}{(1 - x^2)^{3/2}} dx , \tag{A6}$$

$$I_\phi(e) = \int_0^e \frac{x^{\widetilde{\alpha}}}{\left(1 - \delta x^2\right)^{\widetilde{\beta}}} dx , \tag{A7}$$

TABLE II. Parameter estimation errors for equal-mass SMBH binaries. The initial eccentricities e_0 are 10^{-6} (nearly circular), 0.3 and 0.6., the luminosity distance is $D_L = 6.4$Gpc ($z = 1$), and the angular parameters are $\phi_L = 4.724$, $\mu_L = -0.3455$, $\phi_S = 4.642$ and $\mu_S = -0.3185$.

$SMBH$ ($M_\odot$)	e_0/precession	SNR	$\Delta D_L/D_L$ ($\times 10^{-2}$)	$\Delta\mathcal{M}/\mathcal{M}$ ($\times 10^{-6}$)	Δe_0 ($\times 10^{-6}$)	$\Delta\Omega$ ($\times 10^{-6}$)
$10^7 - 10^7$	$e_0 = 10^{-6}$, no prec.	1119	837	105	1794	193
	$e_0 = 10^{-6}$, incl. prec.	2002	538	9.14	1311	77.9
	$e_0 = 0.3$, no prec.	1116	96.2	67.7	222	3.32
	$e_0 = 0.3$, incl. prec.	1984	42.9	9.42	34.7	0.893
	$e_0 = 0.6$, no prec.	1146	31.6	17.4	6.91	2.16
	$e_0 = 0.6$, incl. prec.	1984	17.3	4.95	2.14	0.689
$10^6 - 10^6$	$e_0 = 10^{-6}$, no prec.	1171	192	3.09	1562	13.5
	$e_0 = 10^{-6}$, incl. prec.	1704	168	1.19	1363	9.33
	$e_0 = 0.3$, no prec.	1176	30.6	3.99	7.53	2.00
	$e_0 = 0.3$, incl. prec.	1701	26.0	1.51	3.32	1.00
	$e_0 = 0.6$, no prec.	1200	10.3	3.17	1.18	1.84
	$e_0 = 0.6$, incl. prec.	1712	8.29	1.56	0.917	0.871
$10^5 - 10^5$	$e_0 = 10^{-6}$, no prec.	1924	314	1.03	2595	30.6
	$e_0 = 10^{-6}$, incl. prec.	2183	296	0.958	2365	25.6
	$e_0 = 0.3$, no prec.	1925	33.4	1.30	2.74	0.848
	$e_0 = 0.3$, incl. prec.	2184	26.6	1.16	3.54	0.553
	$e_0 = 0.6$, no prec.	1920	14.3	1.04	0.435	0.678
	$e_0 = 0.6$, incl. prec.	2188	12.0	1.23	0.831	0.520
$10^4 - 10^4$	$e_0 = 10^{-6}$, no prec.	306	746	0.628	4605	239
	$e_0 = 10^{-6}$, incl. prec.	314	697	1.93	4433	189
	$e_0 = 0.3$, no prec.	310	71.2	0.847	1.60	30.3
	$e_0 = 0.3$, incl. prec.	318	62.9	1.80	4.68	29.0
	$e_0 = 0.6$, no prec.	333	30.0	0.539	0.193	28.3
	$e_0 = 0.6$, incl. prec.	341	27.3	0.925	0.356	27.4

with the constants $\alpha = 29/19$, $\beta = -1181/2299$, $\delta = -121/304$, $\widetilde{\alpha} = 11/19$ and $\widetilde{\beta} = 124/2299$. The integrals in Eqs. (A6) and (A7) can be evaluated with the Appell functions which generalize the hypergeometric functions [66, 67]

$$I_t(e) = \frac{19e^{48/19}}{48} F_1\left(\frac{\alpha+1}{2}, \beta, \frac{3}{2}, \frac{\alpha+3}{2}; \delta e^2, e^2\right) \tag{A8}$$

$$I_\phi(e) = \frac{19e^{30/19}}{30}\, {}_2F_1\left(\frac{\widetilde{\alpha}+1}{2}, \widetilde{\beta}, \frac{\widetilde{\alpha}+3}{2}; \delta e^2\right) \ . \tag{A9}$$

To compute the time (ΔT) and phase ($\Delta\Phi$) difference the binary spends between the initial and final eccentricities e_0 and e_1 during its evolution, Eqs. (A4) and (A5) are used,

$$\Delta T = \frac{15}{304\mathcal{M}^{5/3}} \left(\frac{\sigma(e_0)}{2\pi\nu_0}\right)^{8/3} [I_t(e_0) - I_t(e_1)] \ , \tag{A10}$$

$$\Delta\Phi = \frac{15}{304\mathcal{M}^{5/3}} \left(\frac{\sigma(e_0)}{2\pi\nu_0}\right)^{5/3} [I_\phi(e_0) - I_\phi(e_1)] \tag{A11}$$

Figures 11 and 12 show the evolution of time and phase for various initial eccentricities and fixed one-year inspiraling time before the LSO and $10^6 M_\odot$ equal-mass binaries. It can bee seen that the eccentricity changes significantly near the coalescence and the accumulated number of orbit is decreasing for high initial eccentricity.

Appendix B: Stationary Phase Approximation

Consider the waveform $h(t) = \mathcal{A}(t)\cos\Phi(t)$ with $\dot{\mathcal{A}}(t)/\mathcal{A}(t) \ll \dot{\Phi}(t)$ and $\ddot{\Phi}(t) \ll \dot{\Phi}(t)^2$, see e.g. [5], with its Fourier transform as

$$\mathcal{F}\left[\mathcal{A}(t)\cos\Phi(t)\right] = \int_{-\infty}^{\infty} \mathcal{A}(t)\frac{e^{i\Phi(t)} + e^{-i\Phi(t)}}{2} e^{2\pi i t f} dt \ . \tag{B1}$$

To evaluate the Fourier integral one can use the *stationary phase approximation* (SPA). For an arbi-

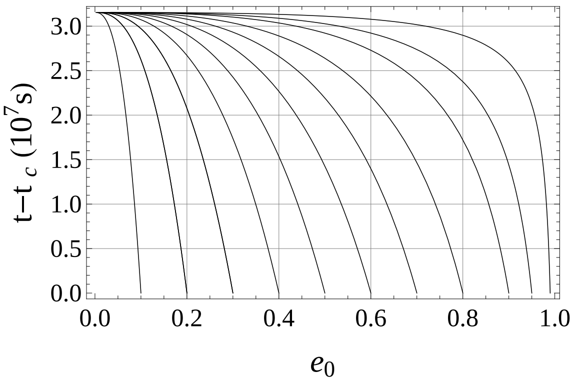

FIG. 11. The evolution of the eccentricity as a function of time (as "lifetime" for the fixed one-year inspiraling time). The eccentricity changes significantly near the coalescence.

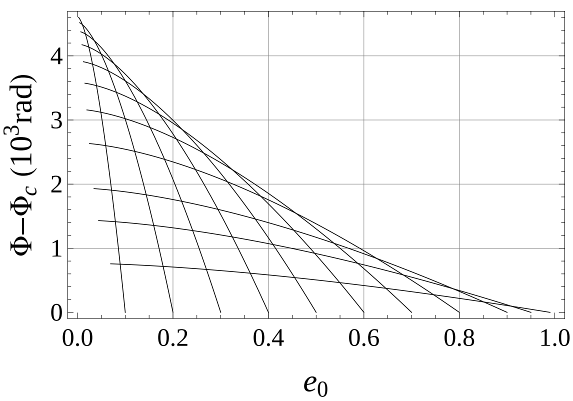

FIG. 12. The evolution of the eccentricity in terms of the phase function for the fixed one-year inspiraling time.

trary function of the time, $\Psi(t)$, $\int_{-\infty}^{\infty} \mathcal{A}(t)e^{i\Psi(t)}dt \simeq \mathcal{A}(\mathcal{T})\sqrt{2\pi/\ddot{\Psi}(\mathcal{T})}e^{i\left(\Psi(\mathcal{T})+\text{sign}\left[\ddot{\Psi}(\mathcal{T})\right]\pi/4\right)}$ where the saddle point $\mathcal{T}$ satisfies $\dot{\Psi}(\mathcal{T})=0$. In Eq. (B1) the $e^{i\Phi(t)}$ terms have no contributions to the saddle point $\mathcal{T}$. Moreover, $\Psi(t) = 2\pi tf - \Phi(t)$ and the stationary phase condition ($\dot{\Psi}(\mathcal{T})=0$) implies that $f=\dot{\Phi}(\mathcal{T})/(2\pi)$. This provides a relation between the Fourier and orbital frequencies. Carrying out this exercise for an eccentric waveform consisting of many widely separated GW harmonics, the corresponding Fourier frequencies are respectively $f_n = n\nu$ and $f_{n\pm} = n\nu \pm \dot{\gamma}/\pi$ for the terms due to pericenter precession. For circular orbits the only nonvanishing term has frequency $f = 2\nu$. Therefore the Fourier transform of harmonic functions with SPA are

$$\mathcal{F}\left[\mathcal{A}(t)\sin\Phi(t)\right] = \frac{\mathcal{A}[f(\mathcal{T})]}{2}\sqrt{\frac{2\pi}{\left|\ddot{\Psi}[f(\mathcal{T})]\right|}}e^{i\left(\Psi[f(\mathcal{T})]+\frac{\pi}{4}\right)}, \tag{B2}$$

$$\mathcal{F}\left[\mathcal{A}(t)\cos\Phi(t)\right] = \frac{\mathcal{A}[f(\mathcal{T})]}{2}\sqrt{\frac{2\pi}{\left|\ddot{\Psi}[f(\mathcal{T})]\right|}}e^{i\left(\Psi[f(\mathcal{T})]-\frac{\pi}{4}\right)}, \tag{B3}$$

where $\Psi\left[f(\mathcal{T})\right] = 2\pi f(\mathcal{T})t\left[\nu(\mathcal{T})\right] - \Phi\left[\nu(\mathcal{T})\right]$ is the phase function and $t\left[\nu(\mathcal{T})\right]$, $\Phi\left[\nu(\mathcal{T})\right]$ are derived from radiation reaction by Eqs. (A4) and (A5).

Following [62] the phase functions for eccentric compact binaries are

$$\Psi_n = 2\pi ft - \Phi_n \ , \tag{B4}$$

$$\Psi_{n\pm} = 2\pi ft - \Phi_{n\pm} \ , \tag{B5}$$

where the functions $\Phi_n, \Phi_{n\pm}$ are defined by Eqs. (12) and (13) and the first time derivatives are expressed as

$$\dot{\Psi}_n = 2\pi f - 2\pi n\nu \ , \tag{B6}$$

$$\dot{\Psi}_{n\pm} = 2\pi f - 2\pi n\nu \mp 2\dot{\gamma} \ . \tag{B7}$$

There are three saddle points t_n, $t_{n\pm}$ following from the stationary phase conditions $\dot{\Psi}_n(t_n) = 0$ and $\dot{\Psi}_{n\pm}(t_{n\pm}) = 0$. It follows that there are three Fourier frequencies for each harmonic of the orbital frequency (denoted by f_n, $f_{n\pm}$). The second time derivatives of the Ψ_n and $\Psi_{n\pm}$ phase functions are

$$\ddot{\Psi}_n = -2\pi n\dot{\nu} \ , \tag{B8}$$

$$\ddot{\Psi}_{n\pm} = -2\pi n\dot{\nu} \mp 2\ddot{\gamma} \ , \tag{B9}$$

where $\ddot{\gamma}$ is the time derivative of $\dot{\gamma}$ induced by gravitational radiation, see Eqs. (10) and (11). Then the phase functions of the waveforms, Eqs. (15) and (16), can be expressed in terms of the time corresponding to the stationary phase and the acceleration of the pericenter precession, formally

$$\Psi_n(f_n) = 2\pi f_n t_n(f_n) - \Phi_n(f_n) \ , \tag{B10}$$

$$\Psi_{n\pm}(f_{n\pm}) = 2\pi f_{n\pm} t_{n\pm}(f_{n\pm}) - \Phi_{n\pm}(f_{n\pm}) \ . \tag{B11}$$

[1] P. L. Bender et al., *LISA Pre-Phase A Report*, 2nd ed. (1998). See http://lisa.jpl.nasa.gov
[2] P. Amaro-Seoane, S. Aoudia, S. Babak, P. Binetruy, E. Berti, et al., (2012), arXiv:1201.3621 [astro-ph.CO].
[3] LISA Science Team, K. Danzmann, *Class. Quant. Grav.* **14**, 1399 (1997).
[4] L. A. Wainstein and V. D. Zubakov, *Extraction of Signals from Noise*, Prentice-Hall, Englewood Cliffs (1962).
[5] L. S. Finn and D. F. Chernoff, Phys. Rev. D **47**, 2198 (1993).
[6] C. Cutler, É. E. Flanagan Phys. Rev. D **49**, 2658 (1994).
[7] K. S. Thorne, Rev. Mod. Phys. **52**, 299 (1980).
[8] C. Cutler, Phys. Rev. D **57**, 7089 (1998).
[9] A. Vecchio, Phys. Rev. D **70**, 042001 (2004).
[10] E. Berti, A. Buonanno, and C. M. Will, Phys. Rev. D **71**, 084025 (2005).
[11] R. Lang and S. A. Hughes, Phys. Rev. D **74**, 122001 (2006).
[12] K. G. Arun, B. R. Iyer, B. S. Sathyaprakash, S. Sinha, and C. van den Broeck, Phys. Rev. D, **76**, id. 104016 (2007).
[13] M. Trias and A. M. Sintes, Phys. Rev. D**77**, 024030 (2008).
[14] R. Lang and S. A. Hughes, Astrophys. J. **677**, 1184 (2008).
[15] S. T. McWilliams, R. N. Lang, J. G. Baker, and J. I Thorpe, Phys. Rev. D**84**, id. 064003 (2011).
[16] D. Holz and S. A. Hughes, Astrophys. J. **629**, 15 (2005).
[17] B. Kocsis, Z. Frei, Z. Haiman, and K. Menou, Astrophys. J. **637**, 27 (2006).
[18] B. Kocsis, Z. Haiman, K. Menou, and Z. Frei, Phys. Rev. D**76**, id. 022003 (2007).
[19] B. Kocsis, Z. Haiman, and K. Menou, Astrophys. J. **684**, 870 (2008).
[20] P. C. Peters and S. Mathews, Phys. Rev. **131**, 435 (1963).
[21] P. C. Peters, Phys. Rev. **136**, B1224 (1964).
[22] P. J. Armitage and P. Natarajan, Astrophys. J. **632**, 921 (2005).
[23] A. I. MacFadyen and M. Milosavljevic, Astrophys. J. **672**, 83 (2008).
[24] J. Cuadra et al., Mon. Not. R. Astron. Soc. **393**, 1423 (2009).
[25] A. Sesana, Astrophys. J. **719**, 851. (2010).
[26] M. Preto, I. Berentzen, P. Berczik, D. Merritt, and R. Spurzem, J. Phys.:Conf. Ser. **154** 012049 (2009).
[27] T. Matsubayashi, J. Makino, and T. Ebisuzaki, Astrophys. J. **656**, 879 (2007).
[28] U. Löckmann, H. Baumgardt, Mon. Not. R. Astron. Soc. **384**, 323 (2008).
[29] L. Wen, Astrophys. J. **598**, 419 (2003).
[30] L. Hoffman and L. Loeb, Mon. Not. Roy. Astron. Soc. **377** , 957 (2007).
[31] N. Seto, Phys. Rev. D**85**, 064037 (2012).
[32] Antonini F. and H. Perets, ApJ in press, arXiv:1203.2938 (2012).
[33] S. Naoz, B. Kocsis, A. Loeb, and N. Yunes, submitted to Astrophys. J., arXiv:1206.4316 (2012).
[34] K. Hattori and Y. Yoshii, Mon. Not. R. Astron. Soc. **408**, 2137 (2010).
[35] D. Merritt and E. Vasiliev, Astrophys. J. **726**, 61 (2011).
[36] P. Amaro-Seoane et al., Class. Quant. Grav., **24**, 113 (2007).
[37] P. Amaro-Seoane, eprint arXiv:1205.5240 (2012).
[38] R. M. O'Leary, B. Kocsis, and A. Loeb, Mon. Not. R. Astron. Soc. **395**, 2127 (2008).
[39] B. Kocsis and J. Levin, Phys. Rev. D**85**, 123005 (2012)
[40] I. Kowalska, T. Bulik, K. Belczynski, M. Dominik and D. Gondek-Rosinska, Astron. and Astrophys. **527**, A70 (2011).
[41] C. Cutler and M. Vallisneri, Phys. Rev. D**76**, 104018 (2007).
[42] K. Martel and E. Poisson, Phys. Rev. D **60**, 124008 (1999).
[43] D. A.Brown and P. J. Zimmerman, Phys. Rev. D**81**, id. 024007 (2010).
[44] E. K. Porter and A. Sesana, *Eccentric Massive Black Hole Binaries in LISA I : The Detection Capabilities of Circular Templates*, submitted to Phys. Rev. D, arXiv:1005.5296 [gr-qc] (2010).
[45] Z. Keresztes, B. Mikóczi, and L. A. Gergely, Phys. Rev. D **72**, 104022 (2005).
[46] A. Klein and P. Jetzer, Phys. Rev. D **81**, 124001 (2010).
[47] A. Gopakumar and G. Schäfer, Phys. Rev. D**84**, id. 124007 (2011).
[48] M. Tessmer and G. Schäfer, Annalen der Physik **523**, 813 (2011).
[49] I. Hinder, F. Herrmann, P. Laguna, and D. Shoemaker, Phys. Rev. D, **82**, id. 024033 (2010).
[50] N. J. Cornish and J. S. Key, Phys. Rev. D 82, 044028 (2010).
[51] N. J. Cornish and E. K. Porter, Class. Quant. Grav. **24**, 5729 (2007).
[52] J. S. Key and N. J. Cornish, Phys. Rev. D **83**, 083001 (2011).
[53] S. A. Hughes, Mon. Not. R. Astron. Soc. **331**, 805 (2002).
[54] L. Barack and C. Cutler, Phys. Rev. D **69**, 082005 (2004).
[55] N. Yunes, K. G. Arun, E. Berti, and C. M. Will, Phys. Rev. D **80**, 084001 (2009).
[56] K. Yagi and T. Tanaka, Phys. Rev. D **81**, 064008 (2010); **81**, 109902(E) (2010).
[57] B. F. Schutz, Nature, **323**, 310 (1986).
[58] H. Wahlquist, Gen. Relativ. Gravit. **19**, 1101 (1987).
[59] V. Pierro, I. M. Pinto, A. D. Spallicci, E. Laserra, and F. Recano, Mon. Not. R. Astron. Soc. **325**, 358 (2001).
[60] M. Tessmer and G. Schäfer, Phys. Rev. D **82** 82, 124064 (2010).
[61] C. Moreno-Garrido, J. Buitrago, and E. Mediavilla, Mon. Not. R. Astron. Soc. **274**, 115 (1995).
[62] C. Moreno-Garrido, J. Buitrago, and E. Mediavilla, Mon. Not. R. Astron. Soc. **266**, 16 (1994).
[63] N. Seto, Phys. Rev. Lett. **87**, 251101 (2001).
[64] A. H. Mroué, H. P. Pfeiffer, L. E. Kidder, and S. A. Teukolsky, Phys. Rev. D **82**, 124016 (2010).
[65] See http://www.srl.caltech.edu/~shane/sensitivity/
[66] V. Pierro, I. M. Pinto, A. D. Spallicci, Mon. Not. R. Astron. Soc. **334**, 855 (2002).
[67] A. Erdélyi, W. Magnus F., Oberhettinger and F. G. Tricomi, *Higher Transcendental Functions, Vol. 1*, New York: Krieger, pp. 222 and 224 (1981).